INTERFACE

royalsocietypublishing.org/journal/rsif

Research

Cite this article: Howsmon DP, Rego BV, Castillero E, Ayoub S, Khalighi AH, Gorman RC, Gorman III JH, Ferrari G, Sacks MS. 2020 Mitral valve leaflet response to ischaemic mitral regurgitation: from gene expression to tissue remodelling. *J. R. Soc. Interface* **17**: 20200098. http://dx.doi.org/10.1098/rsif.2020.0098

Received: 10 February 2020
Accepted: 7 April 2020

Subject Category:
Life Sciences–Engineering interface

Subject Areas:
biomechanics, biomedical engineering, systems biology

Keywords:
mitral valve, ischaemic mitral regurgitation, tissue remodelling, valve interstitial cell, RNA sequencing

Author for correspondence:
Michael S. Sacks
e-mail: msacks@oden.utexas.edu

†Both authors contributed equally to this manuscript.

Electronic supplementary material is available online at https://doi.org/10.6084/m9.figshare.c.4955015.

THE ROYAL SOCIETY PUBLISHING

Mitral valve leaflet response to ischaemic mitral regurgitation: from gene expression to tissue remodelling

Daniel P. Howsmon[1,†], Bruno V. Rego[1,†], Estibaliz Castillero[2], Salma Ayoub[1], Amir H. Khalighi[1], Robert C. Gorman[3], Joseph H. Gorman III[3], Giovanni Ferrari[2] and Michael S. Sacks[1]

[1]James T. Willerson Center for Cardiovascular Modeling and Simulation, Oden Institute for Computational Engineering and Sciences and the Department of Biomedical Engineering, The University of Texas at Austin, Austin, TX, USA
[2]Department of Surgery, Columbia University Irving Medical Center, New York, NY, USA
[3]Gorman Cardiovascular Research Group, Smilow Center for Translational Research, Department of Surgery, Perelman School of Medicine, University of Pennsylvania, Philadelphia, PA, USA

DPH, 0000-0002-7177-1342; BVR, 0000-0002-6315-693X; EC, 0000-0002-2213-5809; SA, 0000-0002-5979-8112; AHK, 0000-0001-8135-3980; GF, 0000-0002-8863-2496; MSS, 0000-0002-2711-8370

Ischaemic mitral regurgitation (IMR), a frequent complication following myocardial infarction (MI), leads to higher mortality and poor clinical prognosis if untreated. Accumulating evidence suggests that mitral valve (MV) leaflets actively remodel post MI, and this remodelling increases both the severity of IMR and the occurrence of MV repair failures. However, the mechanisms of extracellular matrix maintenance and modulation by MV interstitial cells (MVICs) and their impact on MV leaflet tissue integrity and repair failure remain largely unknown. Herein, we sought to elucidate the multiscale behaviour of IMR-induced MV remodelling using an established ovine model. Leaflet tissue at eight weeks post MI exhibited significant permanent plastic radial deformation, eliminating mechanical anisotropy, accompanied by altered leaflet composition. Interestingly, no changes in effective collagen fibre modulus were observed, with MVICs slightly rounder, at eight weeks post MI. RNA sequencing indicated that YAP-induced genes were elevated at four weeks post MI, indicating elevated mechanotransduction. Genes related to extracellular matrix organization were downregulated at four weeks post MI when IMR occurred. Transcriptomic changes returned to baseline by eight weeks post MI. This multiscale study suggests that IMR induces plastic deformation of the MV with no functional damage to the collagen fibres, providing crucial information for computational simulations of the MV in IMR.

1. Background

The fundamental physiological function of the mitral valve (MV) is to facilitate unidirectional blood flow from the left atrium to the left ventricle (LV). Both the MV anterior and posterior leaflets are connected to the papillary muscles via the chordae tendineae, creating an intimate mechanical coupling with the LV [1–3]. MV pathologies are most commonly associated with inadequate leaflet coaptation during systole, which leads to mitral regurgitation (MR) and subsequent retrograde flow into the left atrium. MR is the most common valvular heart disease in developed countries, with an estimated prevalence of 1.7% [4], and is associated with an elevated risk of pulmonary congestion, heart failure and stroke. Whereas primary MR results from an intrinsically diseased valve (e.g. myxomatous disease), secondary MR occurs in response to adverse remodelling of the LV (e.g. due to ischaemic cardiomyopathy) as a result of the intimate coupling between the MV and LV. Ischaemic MR (IMR), secondary MR due to ischaemic cardiomyopathy, is present after myocardial infarction (MI) in 40–50% of cases [5,6] (with moderate/severe IMR in 12–19% of cases [5,7]). LV

remodelling induces IMR, which leads to further LV remodelling [8], creating a positive feedback loop that doubles the rate of cardiac mortality post MI when IMR is present [7,9,10].

IMR is treated surgically either through MV repair or replacement, with repair currently the preferred method. This is based on the assumption that preserving the normal cardiac LV–MV structural interactions is beneficial. Early reports regarding MV replacement revealed a higher 30-day postoperative risk of death compared with valve repair (OR = 2.52, 95%CI 1.91–3.34) for severe IMR [11]. Moreover, repair without recurrent IMR results in superior LV volume reduction over replacement, but this LV volume reduction vanished if IMR recurred [12]. However, more recent studies in patients with severe IMR report similar death rates for repair versus chordal-sparing replacement, but the IMR recurrence rate was much higher in the repair group (32.6% versus 2.3%) at 1 year [12] and (58.8% versus 3.8%) at 2 years [13]. Newer, less invasive surgical techniques, such as the MitraClip, promise to address both the safety of the procedure and the IMR recurrence rate [14]. However, long-term outcomes for these approaches remain unknown. Regardless of the specific intervention strategy, the state of the MV leaflet tissue up to and at the time of intervention remains poorly understood.

Although IMR is classically depicted as functional (i.e. without intrinsic changes to the MV), accumulating evidence suggests that the MV undergoes substantial remodelling post MI. Related studies have reported that total MV area, MV thickness and collagen content increased in both the human MV [15] and ovine models of IMR [16,17]. Furthermore, in an ovine model with tethered leaflets to emulate the effects of IMR without the confounding effects of LV ischaemia, the MV exhibited increases in area and thickness [18], indicating that leaflet tethering is probably driving this remodelling. These findings also agree with computed tomography assessments that observe thickened leaflets and mitral stenosis in a subset of repaired MVs [19]. We have recently demonstrated in an ovine model that post MI the MV leaflets are permanently distended in the radial direction, with the magnitude and rate of distension varying regionally over the leaflet surface [20]. The driver underlying these events appears to be changes to the attachment geometry of the MV; specifically, annular dilation and papillary muscle distension. This continued MV remodelling in IMR is thought to underlie reported repair failures [21]. In order for novel surgical methods, especially less invasive ones, to be developed that mitigate the effects of MV and LV remodelling to enhance surgical interventions, a better understanding of MV remodelling in IMR is needed.

Clearly, a better understanding of MV remodelling in IMR directly ties into the clinical success of current surgical interventions. As in all heart valves, the valve interstitial cells (VICs) are the primary drivers of valve tissue growth and remodelling in response to both biochemical and mechanical stimuli [22]. In a recent study, MV leaflet tissue culture in a circumferentially oriented strip bioreactor after 48 h of cyclic strain significantly upregulated many genes related to extracellular matrix (ECM) remodelling [23]. Altered mechanical loads following undersized ring annuloplasty and/or papillary muscle approximation also show differences in several genes related to ECM remodelling [24]. This feedback interaction between VICs and their micro-mechanical environment and the way this scales to the levels of the tissue and organ (valve and ventricle) warrant further investigation, especially in the context of IMR.

Although recent reports have continued to shed light on the MV remodelling processes post MI, either unaltered [20,25,26] or in the context of various interventions [19,24,27], fundamental questions regarding MV remodelling in IMR remain. In particular, detailed analyses of the functional physiological behaviours of the post MI MV necessary for informing advanced computational simulations of patient-specific surgical procedures remain lacking. At the underlying subcellular response level, individual genes/proteins (e.g. [25,27]) or gene panels related to a single process [24] have been investigated, but there has not been a transcriptomics study that investigates all genes/processes that change in response to IMR *in vivo*. Transcriptomics provides an unbiased approach for investigating the importance of individual genes/processes in the context of global gene expression, potentially uncovering novel genes that would otherwise be overlooked by deciding which genes should be investigated *a priori*.

The present study thus sought to address these shortcomings through a detailed investigation of the impact of IMR at the transcriptomic, cellular and tissue levels in an established ovine model of IMR. MV leaflet tissue explants were evaluated to assess the effects of IMR, including changes in the leaflet tissue mechanical response, quantitative histology to investigate the ECM, and VIC nuclear aspect ratio (NAR) to quantify cell-level geometric changes, which have been associated with VIC biosynthetic levels. In addition, RNA sequencing was used to quantify global gene expression changes post MI in IMR and normal groups. By connecting functional behaviour of the MV leaflets at the highest scale down to changes in gene expression at the lowest scale, this study provides crucial knowledge for designing next-generation surgical devices and suggesting possible points of pharmaceutical intervention to improve the current dismal clinical outcomes for treating IMR.

2. Methods

2.1. Ischaemic mitral regurgitation ovine model

All animal protocols used in this study were approved by the University of Pennsylvania's Institutional Animal Care and Use Committee and complied with the National Institute of Health's guidelines for the care and use of laboratory animals (NIH Publication 85–23, revised 1996). The University of Pennsylvania, with the supervision of the School of Veterinary Medicine, maintains a full-service vivarium facility operated by the University Laboratory Animal Research (ULAR) organization. The vivarium is directly adjacent to the laboratory's operating room suite.

IMR was induced in adult (30–40 kg) Dorset sheep, randomized by sex, raised for laboratory work and supplied by commercial vendors following established procedures [28–30]. Briefly, sheep were anaesthetized with intravenous sodium thiopental (10–15 mg kg^{-1}), intubated and ventilated with isoflurane (1.5–2%) and oxygen. Surface electrocardiogram (ECG), arterial blood pressure and other vital signs were continuously monitored throughout the duration of the procedure. IMR was induced by a thoracotomy to facilitate ligation of the second and third obtuse marginal branches of the circumflex coronary artery. Permanent occlusion of these arteries reliably results in a transmural posterior MI that includes the entire posterior papillary muscle and involves approximately 20% of the LV mass, causing a gradual onset of severe IMR within eight weeks. The eight-week time point is an accepted duration wherein all major ventricular remodelling has occurred and has been routinely used for studying IMR [18,24,31–34]. Surgical interventions can occur over a wide range

of time points, from soon after MI to many months afterwards. Our experimental design thus captures the most relevant time frame, although very long-term responses remain unknown. The degree of MR was assessed with echocardiography. MV leaflets were collected and flash-frozen at pre-MI as well as four and eight weeks post MI. All sheep were euthanized by an overdose of KCl and sodium thiopental while under general anaesthesia. The animals were pronounced dead only after ECG silence had been demonstrated for 3–5 min and cardiac arrest was visibly confirmed. This technique has been approved by the University of Pennsylvania Institutional Animal Care and Use Committee and is consistent with the recommendations of the American Veterinary Medical Association Guidelines on Euthanasia. Leaflets from one subset of 14 animals were used for mechanical testing (pre-MI, $n = 6$; eight weeks post MI, $n = 8$) and tissue characterization via histology and electron microscopy (pre-MI, $n = 3$; eight weeks post MI, $n = 8$). All of the animals in this first subset displayed low-grade IMR at eight weeks post MI. Leaflets from a second subset of 13 animals (pre-MI, $n = 4$; four weeks post MI, $n = 5$; eight weeks post MI, $n = 4$) were used for RNA isolation and quantification. Half of the animals at four and eight weeks post MI exhibited low-grade IMR, with the other half exhibiting no observable IMR. No animals exhibited IMR at the pre-MI time point.

2.2. Mitral valve leaflet tissue mechanical evaluation

2.2.1. Biaxial mechanical testing

As MV leaflets are relatively thin, their mechanical behaviour has been extensively characterized using planar biaxial mechanical testing methods [35–37]. In the present study, we used our established experimental biaxial system to evaluate the mechanical behaviours of $1 \times 1\ \text{cm}^2$ specimens extracted from the upper mid-regions of 14 ovine MV anterior leaflets (pre-MI, $n = 6$; eight weeks post MI, $n = 8$) following established procedures [36,37]. Specifically, each specimen was loaded to an approximate end-systolic peak leaflet tissue stress of approximately 200 kPa, while setting the following circumferential-to-radial ratios of the first Piola–Kirchhoff stress tensor components $P_{CC} : P_{RR}$ to values of 1:2, 3:4, 1:1, 4:3 and 2:1. For each specimen, the right Cauchy–Green deformation tensor $\mathbf{C}$ and second Piola–Kirchhoff stress tensors $\mathbf{S}$ were computed at each instant of loading. For clarity, an illustration of the location of the samples for mechanical testing and histological analysis are provided in figure 1.

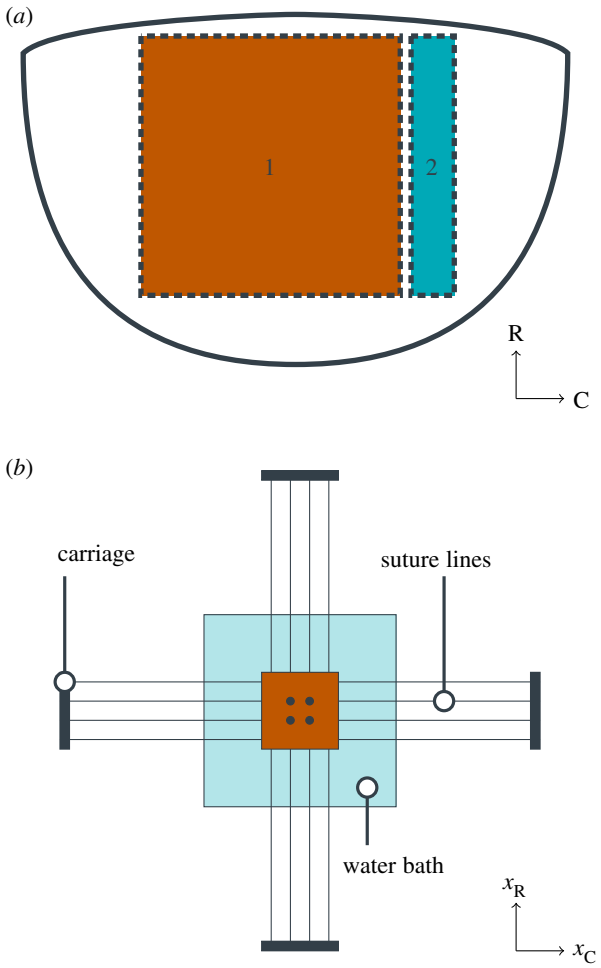

Figure 1. Tissue preparation for mechanical testing and tissue-level experiments. (*a*) Illustration of tissue explant with radial (R) and circumferential (C) directions used for mechanical testing (region 1) and that used for histology (region 2). (*b*) Illustration of the biaxial mechanical testing apparatus, with four centrally located fiducial markers, sutures mounting the tissue sample, and displacements x_R and x_C in the radial and circumferential directions, respectively.

2.2.2. Constitutive model formulation

One of the major goals of the present study was to reveal changes in *intrinsic* mechanical behaviour of the primary structural ECM constituent, the collagen fibres. However, this cannot be derived directly from the mechanical data, since alterations in tissue-level mechanical behaviour can be a combined result of changes in collagen fibre stiffness and its physical architecture. To separate these two effects, we used the following structural constitutive (material) model specialized for the MV leaflets. Details of the model were extensively presented in [38]. Briefly, a meso-scale (i.e. at the level of the fibre, 10–100 µm in length) structural constitutive model for MV leaflet tissues was developed. The model is predicated on the assumption of affine fibre kinematics [39]. Fibre kinematic models of this type have been used previously to describe changes in mitral valve structure under different loading conditions [38–40] and in the non-pathological remodelling conditions of pregnancy [41]. Although the original model was developed with layer-specific contributions separately modelled, we homogenized all four layer contributions into a single collagen-rich effective structure, simplifying the approach and recognizing that the highly collagenous fibrosa layer dominates the mechanical behaviour. Moreover, for the present study, we are mainly interested in the effective adaptations of the dominant collagen fibre network post IMR. We further assumed that

1. The collagen fibres are linearly elastic, with a strain energy function $\Psi_f = (\gamma_c/2)(\lambda_{\mathbf{n}}/\lambda_s - 1)$, where γ_c is the collagen fibre modulus, $\lambda_{\mathbf{n}}$ is the local tissue stretch in the $\mathbf{n}$ direction and λ_s is the collagen fibre slack stretch.
2. The collagen fibre orientation distribution function $\Gamma_\theta(\theta)$ for the collagen fibre was known, and follows a Beta distribution bounded by $\theta \in [-\pi/2, \pi/2]$ with mean μ_θ and standard deviation σ_θ. Moreover, Γ_θ can be mapped from the reference to the current state using affine fibre kinematics, as done previously [38–41].
3. The recruitment of the collagen fibres is modelled by a second Beta distribution $\Gamma_s(\lambda_s)$ with mean μ_s and standard deviation σ_s, and is bounded by $\lambda_s \in [1, \lambda_s^{ub}]$, where λ_s^{ub} is the upper bound slack stretch.
4. The total tissue strain energy is the sum of the contributions of each individual collagen fibre.
5. The remaining content of the tissue is a compliant, incompressible matrix that can be modelled as a neo-Hookean material with shear modulus 5 kPa.
6. The shear modulus for the neo-Hookean modelled matrix is assumed not to change with remodelling, as supported by inspection of the low-stress region of the mechanical data. This assumption is based on our related work on the bioprosthetic heart valve fatigue model [42].

The expression for the second Piola–Kirchhoff stress tensor **S** as a function of the tissue-level deformation tensor **C** is given by

$$\mathbf{S}(\mathbf{C}) = \bar{\gamma}_c \int_{-\pi/2}^{\pi/2} \frac{\Gamma_\theta(\theta \mid \mu_\theta, \sigma_\theta)}{\lambda_\mathbf{n}} \left[\int_1^{\lambda_\mathbf{n}} \frac{\Gamma_s(\lambda_s, \theta \mid \mu_s, \sigma_s, \lambda_s^{ub})}{\lambda_s} \left(\frac{\lambda_\mathbf{n}}{\lambda_s} - 1 \right) \mathrm{d}\lambda_s \right] \mathbf{n}(\theta) \otimes \mathbf{n}(\theta)\, \mathrm{d}\theta, \tag{2.1}$$

where $\bar{\gamma}_c$ is the estimated effective collagen fibre modulus, $\lambda_\mathbf{n} = \sqrt{\mathbf{n}(\theta) \cdot \mathbf{C}\mathbf{n}(\theta)}$ is the tissue stretch along the direction vector $\mathbf{n}(\theta)$. Owing to the inherent correlations between the mass fraction of collagen ϕ_c and the collagen fibre modulus γ_c, we instead chose to focus on the effective collagen fibre modulus $\bar{\gamma}_c = \phi_c \gamma_c$, as done previously [43].

This basic formulation was slightly modified to accommodate the needs of the present study as follows. Although in normal MV leaflet tissues the collagen fibre slack stretch λ_s was found to be essentially independent of angle [38], prolonged periods of IMR have been shown to induce large changes in MV leaflet dimensions, especially in the radial direction [20]. Such radially biased directional changes in leaflet shape are likely to induce parallel alterations in the collagen fibre architecture, making Γ_s dependent on θ. To account for this effect, and distinguish it from structural changes due to active remodelling, we introduced a radial pre-stretch parameter λ_R, and used it as follows. At any angle θ, the corresponding IMR-induced radial pre-stretch is $\lambda_\mathbf{n}^{ps}(\theta) = \sqrt{\cos^2\theta + \lambda_R^2 \sin^2\theta}$. Therefore, with respect to the reference configuration for mechanical testing, the angle-specific mean, standard deviation and upper bound of Γ_s are $\mu_s/\lambda_\mathbf{n}^{ps}$, $\sigma_s/\lambda_\mathbf{n}^{ps}$ and $\lambda_s^{ub}/\lambda_\mathbf{n}^{ps}$, respectively. Key features of this approach are that (i) the model parameters have a *direct physical meaning* and (ii) we can separate changes in intrinsic collagen fibre properties (via $\bar{\gamma}_c$) from changes in the collagen fibre architecture (via Γ_θ and Γ_s). This allows us to address the question of whether changes due to IMR alter the intrinsic collagen fibres (e.g. due to fatigue damage or active cell-mediated remodelling), the fibrous structure, or both.

2.2.3. Parameter estimation

Details of the parameter estimation methods used have been detailed previously [38,41]. Briefly, we first examined the equibiaxial stress protocol ($P_{CC} : P_{RR} = 1 : 1$), which approximates the *in vivo* loading state of the MV. Once a reliable estimate of the parameters was obtained for this protocol, all protocols (1:2, 3:4, 1:1, 4:3 and 2:1) were estimated via the differential evolution algorithm using the existing parameters as the initial guess. Parameter estimation was performed using a custom program written in Mathematica (Wolfram Research Corp.).

2.3. Histology

2.3.1. Sample preparation

Tissue preparation for histology has been described previously [44,45]. Briefly, samples from MV anterior leaflets (both pre-MI and eight weeks post MI) were fixed with 10% buffered formalin, embedded in paraffin, cut into 5 µm sections, and mounted on glass slides. Slides were then stained with either Movat's pentachrome for visualization of collagen (yellow-orange), glycosaminoglycans (GAGs; light blue) and elastin (dark purple) or haematoxylin and eosin (H&E) for determination of cell density and nuclear geometry. Slides were imaged using a light microscope at 4 ×, 10 × and 20 × magnification (Leica, Wetzlar, Germany).

2.3.2. Quantitative analysis

The relative presence and distribution of each ECM constituent was quantified directly from the resulting images using a pixel-wise colour analysis protocol, extended from methods presented previously [46]. First, the Movat image was converted from a red–green–blue (RGB) format to a hue saturation value (HSV) format. Then, the hue distribution of the tissue-occupied pixels was fitted to a three-component wrapped Gaussian mixture model via maximum-likelihood estimation.

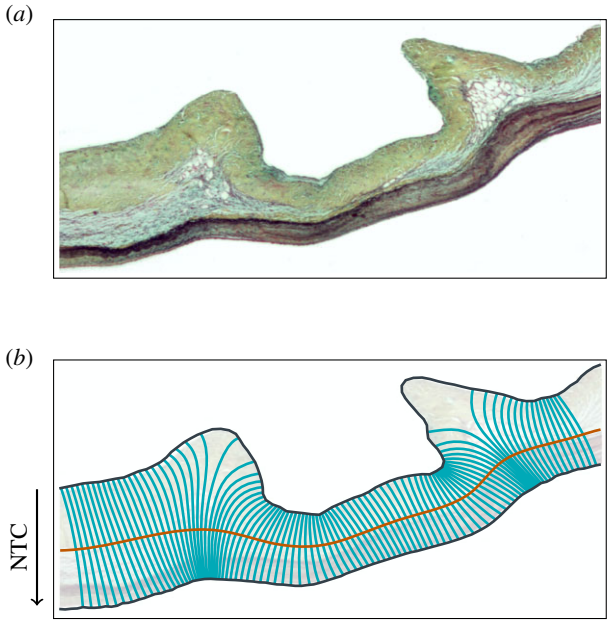

Figure 2. Example of (*a*) a Movat stained sample and (*b*) the corresponding conformal coordinate system with the direction of the NTC.

To describe the distribution of collagen, GAG and elastin mass fractions through the thickness of the leaflet, the tissue-occupied region of each Movat image was transformed to a rectangular domain using a conformal (locally angle-preserving) map such that coordinate directions in the new domain represent the circumferential and transmural directions of the leaflet (figure 2), similar to the characterization of thickness in [47]. This was accomplished through the following procedure. First, the top and bottom boundaries of the tissue region were determined automatically using the saturation mask previously defined to isolate the tissue-occupied region and traced from end to end. Second, local circumferential direction vectors on the boundaries were defined as the unit tangent to the boundary at each point. Third, the circumferential direction vector components were interpolated using a two-dimensional spline function to define the circumferential vector field everywhere within the tissue region. Finally, transmural direction vectors were determined through a 90° rotation of the local circumferential direction. Streamlines of the transmural vector field were then traced from boundary to boundary and discretized with segments of equal arc length, in order to express the thickness-dependent variation in tissue composition with respect to a normalized transmural coordinate (NTC). Transmural tracing was performed sequentially at circumferential locations that were equally spaced halfway through the tissue thickness (defined by the midpoints of the traced transmural streamlines, in an arc length sense).

Since the ECM compositions (in $\mathbb{R}^3$) are constrained such that they sum to unity, the mass fractions were transformed to an orthonormal coordinate system in $\mathbb{R}^2$ as described in [48]. Anderson–Darling tests for normality and Hotelling's T^2 test for differences in location between two distributions were then carried out in the orthonormal coordinate space.

2.3.3. Determination of the nuclear aspect ratio

H&E-stained slides, which provide a sharp contrast between nuclei and the surrounding collagen fibres, were used to

determine MVIC NAR. A custom-written Matlab (MathWorks, Inc., Natick, MA, USA) script was used to automatically detect and fit ellipses to 10 nuclei in each H&E image and the NAR of each MVIC was then calculated as the ratio between the major and minor radii of the corresponding ellipse.

2.4. RNA sequencing workflow

2.4.1. RNA isolation

Isolation of total mRNA was performed using the RNeasy mini kit (Qiagen, Valencia, CA, USA). 1% β-mercaptoethanol was added to the lysis buffer and 30 mg of previously flash-frozen tissue was homogenized with a TissueRuptor (Qiagen). Isolated RNA purity was preliminarily assessed on a NanoDrop spectrophotometer (NanoDrop Technologies, Wilmington, DE, USA). RNA concentration was measured on a Qubit 2.0 fluorometer (Invitrogen, Whaltham, MA, USA). RNA integrity assessment was performed on an Agilent Bioanalyzer 2100 using a Nano 6000 assay kit (Agilent Technologies, Santa Clara, CA, USA). An RNA integrity number (RIN) greater than 7.1 was considered the minimum requirement for library preparation. RNA from one anterior leaflet did not meet this requirement and was removed from analysis. All remaining samples displayed RINs >8.6.

2.4.2. RNA library construction and transcriptome sequencing

RNA library preparation and sequencing was performed at Novogene (Sacramento, CA, USA). RNA quality control by 1% agarose gels and Agilent Bioanalyzer 2100 was repeated before library construction. A total amount of 1 µg RNA per sample was used as input material for the RNA sample preparations. Sequencing libraries were generated using an NEBNext Ultra RNA Library Prep Kit for Illumina (NEB, USA) following the manufacturer's recommendations and index codes were added to attribute sequences to each sample. Briefly, mRNA was purified from total RNA using poly-T oligo-attached magnetic beads. Fragmentation was carried out using divalent cations under elevated temperature in NEBNext First Strand Synthesis Reaction Buffer (5×). First strand cDNA was synthesized using random hexamer primer and M-MuLV reverse transcriptase (RNase H). Second strand cDNA synthesis was subsequently performed using DNA polymerase I and RNase H. Remaining overhangs were converted into blunt ends via exonuclease/polymerase activities. After adenylation of 3′ ends of DNA fragments, NEBNext Adaptor with hairpin loop structure was ligated to prepare for hybridization. In order to select cDNA fragments of preferentially 150–200 bp in length, the library fragments were purified with an AMPure XP system (Beckman Coulter, Beverly, MA, USA). Three millilitres of USER enzyme (NEB, USA) was used with size-selected, adaptor-ligated cDNA at 37°C for 15 min followed by 5 min at 95°C before polymerase chain reaction (PCR). PCR was performed with Phusion High-Fidelity DNA polymerase, universal PCR primers, and Index (X) Primer. Finally, PCR products were purified (AMPure XP system) and the library quality was assessed on the Agilent Bioanalyzer 2100 system. The clustering of the index-coded samples was performed on a cBot Cluster Generation System using PE Cluster Kit cBot-HS (Illumina) according to the manufacturer's instructions. After cluster generation, the library preparations were sequenced on an Illumina platform and 125 bp/150 bp paired-end reads were generated.

2.4.3. Data preprocessing

Raw reads (in FASTQ format) were processed with Perl scripts. Low-quality reads and those containing adapters or poly-N sequences were removed from raw data. The *Ovis aries v3.1* reference genome was obtained from Ensembl (release 76). The index of the reference genome was built using Bowtie (v. 2.2.3) and paired-end reads were aligned to the reference genome using TopHat (v. 2.0.12). HTSeq (v. 0.6.1) was used to count the read numbers mapped to each gene.

2.4.4. Annotation, statistical modelling, and gene set enrichment analysis

All annotation and analysis was performed within BioConductor [49]. Genes were annotated with NCBI Entrez IDs, gene symbols, human homologue Entrez IDs, and human homologue gene symbols using biomaRt [50]. Statistical modelling was performed with DESeq2 [51] with shrinkage of $\log_2$ fold changes provided by the 'apeglm' method [52]. Differential expression (single model) was assessed with a Wald test, whereas the comparison of two (nested) models was assessed with a likelihood ratio test (LRT). Multiple hypothesis correction was performed by controlling the false discovery rate (FDR) via Benjamini–Hochberg, resulting in the reported adjusted p-values [53]. Gene set enrichment analysis [54] was performed with the Reactome database [55,56], where genes were described by human homologue Entrez IDs because Reactome does not currently support analysis for sheep. Genes were ranked by their $\log_2$ fold change after shrinkage. Multiple hypothesis correction was again performed by controlling the FDR via Benjamini–Hochberg [53].

2.4.5. Data availability

All data for the RNA-seq experiments presented in this publication have been deposited in NCBI's Gene Expression Omnibus [57], in compliance with the Minimum Information about a high-throughput nucleotide SEQuencing Experiment (MINSEQE) guidelines, and are accessible through GEO Series accession number GSE139921 (www.ncbi.nlm.nih.gov/geo/query/acc.cgi?acc=GSE139921).

3. Results

3.1. Mechanical responses

Consistent with previous studies [35–37,58], leaflets from pre-MI MVs exhibited pronounced anisotropy and nonlinearity, with greater extensibility in the radial direction than in the circumferential direction (radial peak strain: 18.7% ± 4.7%; circumferential peak strain: 2.9% ± 0.8%). Interestingly, substantial radial stiffening completely eliminated this anisotropy in the eight-week post MI group, on average (radial peak strain: 4.9% ± 1.3%; circumferential peak strain: 5.1% ± 0.6%) (figure 3; electronic supplementary material, figure 1).

Parameter estimates obtained from the structural constitutive model (equation 2.1) suggested that the observed changes in mechanical properties can be attributed predominantly to MI-induced *permanent* radial distension. Specifically, a statistically significant difference between pre-MI and eight weeks post MI groups was only detected in the λ_R parameter, which estimated post MI radial distension. Our results suggest that collagen fibre crimp is largely independent of angle in pre-MI leaflets (i.e. $\lambda_R \approx 1$), consistent with previous findings [38]. Notably, the estimated mean increase in λ_R from pre-MI to eight weeks post MI (9 ± 2%; table 1) agreed well with the reported changes in radial length in previous echocardiography-based measurements of radial leaflet lengthening post MI [20], where the central region of the anterior leaflet was reported to distend about 10% after eight weeks. Interestingly, no differences in effective collagen fibre modulus ($\bar{\gamma}_c$), collagen fibre crimp other than λ_R (μ_s, σ_s, λ_{ub}), or collagen fibre orientation (μ_θ, σ_θ) were

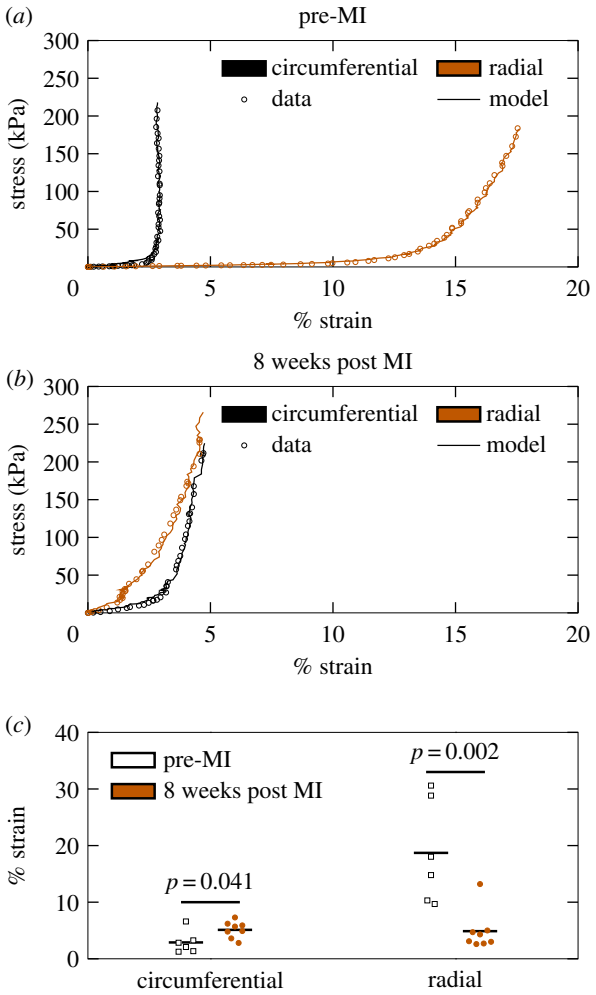

Figure 3. Biaxial mechanical testing results indicate a loss of mechanical anisotropy at eight weeks post MI. Representative stress/strain curves for (*a*) pre-MI and (*b*) eight weeks post MI specimens, with every third datum point plotted to facilitate visualization. (*c*) Strains at 200 kPa for all specimens tested (pre-MI, $n = 6$; eight weeks post MI, $n = 8$). Groups were compared with a Student's *t*-test.

observed. Therefore, the plasticity observed here is attributed to the non-fibrous components of the ECM.

3.2. Extracellular matrix composition at eight weeks post MI

Quantitative histology indicates significant alterations in the overall ECM composition (p-value ± 0.001), with generally decreased GAG mass fraction and increased collagen mass fraction at eight weeks post MI (figure 4). Quantifying NAR from H&E stained slides revealed a decrease in observed NAR from 2.8883 ± 0.1025 to 2.4162 ± 0.1327 (p-value = 0.0963) at eight weeks post MI. This suggests that alterations at the tissue scale in both mechanical and material properties propagate down to mechanical microenvironment-induced MVIC geometric changes.

3.3. Gene expression

The observed changes in tissue mechanical properties and MVIC geometry in samples with MR at eight weeks post MI prompted us to investigate changes in the time course of gene expression in samples with and without MR post MI. A second set of leaflets were processed for RNA-seq, with samples available at pre-MI (without MR), four weeks post MI without MR, four weeks post MI with MR, eight weeks post MI without MR and eight weeks post MI with MR. Since including the interaction between MR and eight weeks post MI did not explain the data better than only including an effect for eight weeks post MI (0 genes, LRT, adjusted p-value <0.1), all samples regardless of IMR status were lumped at the eight weeks time point. All of the genes with an adjusted p-value of ≤0.1 for $\beta_1^{(i)}$, $\beta_2^{(i)}$ or $\beta_3^{(i)}$ in the final model are presented in figure 5. Although many genes have altered expression at four weeks post MI, most genes returned to baseline expression at eight weeks post MI.

Table 1. Summary of parameter estimates from mechanical data.

parameter	pre-MI	8 weeks post MI	*p*-value
$\bar{\gamma}_c$ (MPa)	171 ± 22	178 ± 12	0.76
μ_s	1.10 ± 0.01	1.09 ± 0.01	0.53
σ_s	0.025 ± 0.006	0.021 ± 0.003	0.50
λ_s^{ub}	1.16 ± 0.02	1.14 ± 0.01	0.41
λ_R	0.98 ± 0.01	1.07 ± 0.01	0.0003
μ_θ (deg)	−6.3 ± 10.7	1.9 ± 5.6	0.47
σ_θ (deg)	19.5 ± 5.5	23.6 ± 1.4	0.43

Although large changes in expression for individual genes may significantly impact cellular processes, small changes in many genes within a single unifying biological process are often much more indicative of changes in cell phenotype [54]. Therefore, gene set enrichment analysis (GSEA) [54] using gene sets pre-defined in the Reactome database [55] was used to investigate significant collections of genes. Ranking all genes by β_1, the differential expression due to eight weeks post MI alone resulted in four pathways with significant alterations (adjusted p-value <0.1); however, the core enrichment for all of these pathways consisted of a single gene, *CXCL9*.

Instead, ranking all genes by β_2, the differential expression due to the presence of MR at four weeks post MI resulted in significant differences (adjusted p-value<0.1) in 27 pathways (electronic supplementary material, table 1), of which downregulation of 'extracellular matrix organization' and 'ECM proteoglycans' were among the most significant differences at the level of gene expression. 'Collagen chain trimerization', 'collagen biosynthesis and modifying enzymes' and 'collagen degradation' are also significantly downregulated, agreeing with the increased collagen mass fraction at the tissue level. Finally, 'smooth muscle contraction' is significantly decreased in agreement with the decrease in NAR found through quantitative histology. Together, these gene-level results suggest that most changes in gene expression have returned to baseline by eight weeks post MI and changes in gene expression between samples with and without MR at four weeks post MI are primarily tied to the changes observed in ECM synthesis and remodelling observed at the tissue level.

4. Discussion

4.1. Main findings

The present study and the *in vivo* results reported in [20] characterize the multiscale effects of IMR on the MV

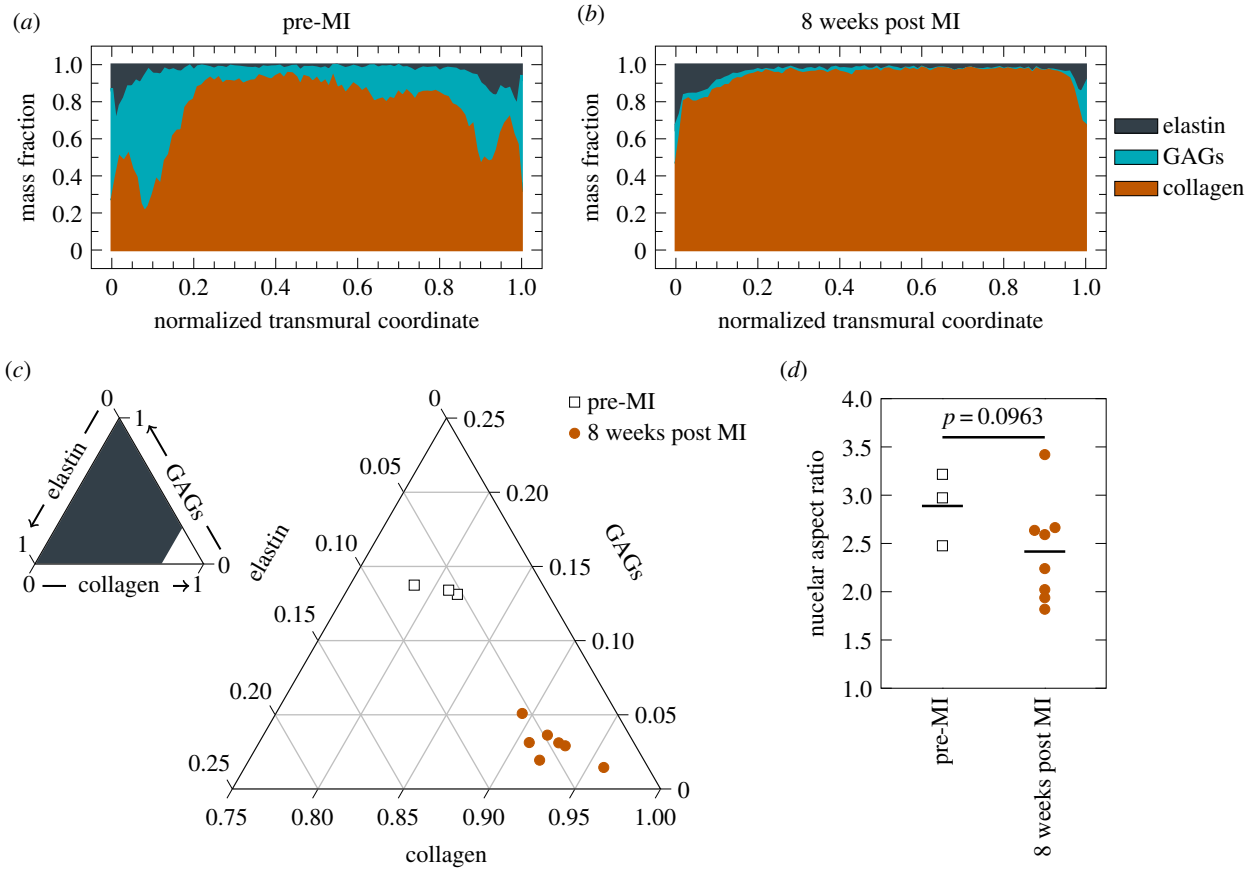

Figure 4. Leaflet compositional changes. Transmural distribution of ECM constituents (*a*) pre-MI versus (*b*) eight weeks post MI. (*c*) Overall composition change of pre-MI ($n = 3$) versus eight weeks post MI ($n = 8$). Groups compared with a Hotelling's T^2 test in the orthonormal coordinate system in $\mathbb{R}^2$ described in the Methods. (*d*) NAR changes pre-MI ($n = 3$) versus eight weeks post MI ($n = 8$). Groups compared with a Student's *t*-test.

(illustrated in figure 6), largely driven by LV wall thinning and dilation, which tether the MV leaflets. With respect to the MV, leaflet tethering induces a prominent *plastic* radial deformation that also alters leaflet biomechanical behaviour. At the cellular level, MVICs appear slightly rounder and transcriptomics points to potential immune cell infiltration, in agreement with previous reports [25]. Furthermore, others have observed endothelial mesenchymal transition (EndMT) in valve endothelial cells (VECs) [25]. Finally, at the gene level, Yes associated protein (YAP) mechanotransduction is prominent at four weeks post MI. Genes regulating ECM organization are downregulated in samples that have experienced IMR at four weeks post MI compared with samples that did not experience IMR. Gene expression is indistinguishable from baseline at eight weeks post MI, indicating that we are only observing the initial MVIC response to IMR. Each scale is further discussed in the text that follows.

4.2. Changes in mechanical behaviour

The mechanical behaviour of the MV anterior leaflets was found to be substantially altered at eight weeks post MI. Specifically, at eight weeks post MI, the radial peak strain significantly decreased, indicating a complete loss of mechanical anisotropy. These *in vitro* results are consistent with the *in vivo* conclusions that leaflet tethering has a larger effect on MV remodelling than annular dilation [20]. The constitutive model (equation 2.1) results (table 1) revealed some interesting trends. First, we noted that neither Γ_θ nor Γ_s changed between the pre- and post MI groups. The only structural parameter that changed was λ_R by approximately 9% strain. That is, radial distension resulting from persistent leaflet tethering induced the more radially oriented fibres to straighten, and thus they are recruited at lower levels of strain with respect to the leaflet's updated unloaded configuration [3,38,60]. Moreover, no difference in effective collagen modulus $\bar{\gamma}_c$ due to IMR was observed (table 1). Thus, at the effective fibre level, there appeared to be neither damage nor augmentation by active remodelling of the collagen fibres and changes in mechanical properties appear to be entirely attributable to the reorientation and straightening of the collagen fibre network in IMR at eight weeks post MI. Given the lack of change in collagen modulus, and that the changes in tissue mechanical behaviours were explained by changes in the collagen fibre structure alone, it appears that the source of the tissue-level plasticity is in the non-fibrous ECM. This may be exacerbated by the decrease in GAG content (figure 4*a–c*).

4.3. Changes in mitral valve interstitial cell shape and gene expression reveal both mitral valve interstitial cells and immune cell responses to ischaemic mitral regurgitation

We start by examining the changes in MVIC shape. We focus on this key metric as we have identified MVIC NAR as a key indicator of MVIC biosynthetic behaviour [23]. The observed

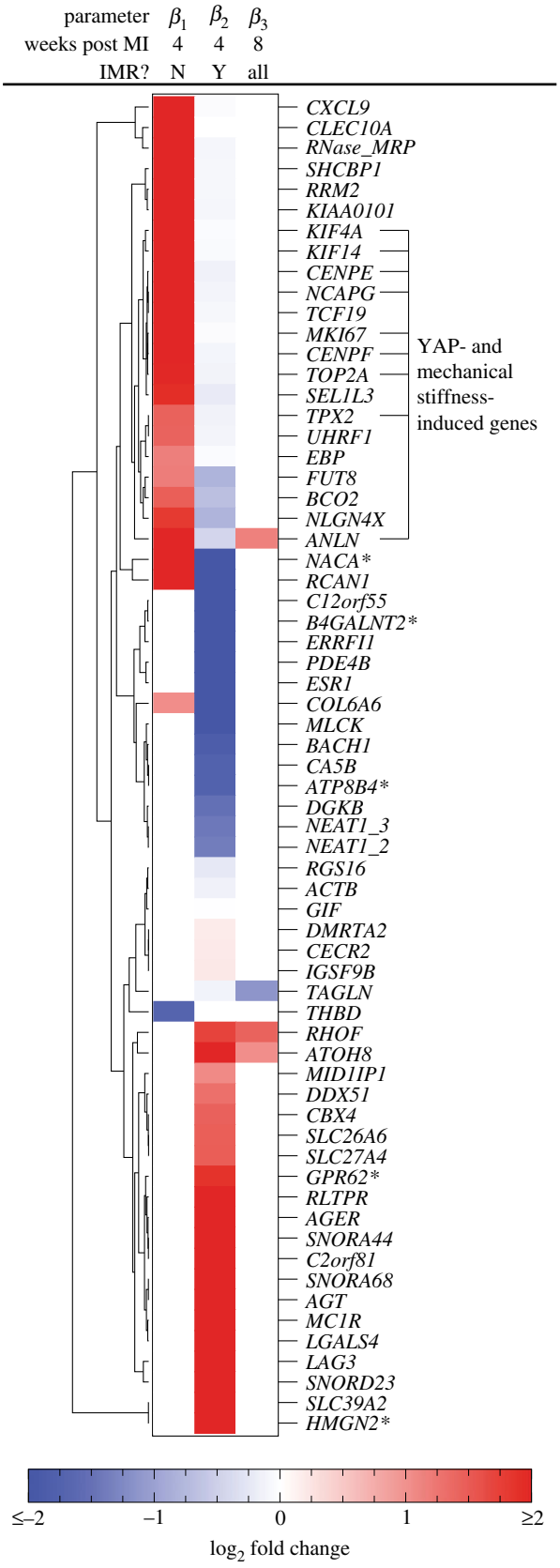

Figure 5. Heatmap of log $_2$ fold changes for genes with a *p*-value of ≤ 0.1 (Wald test with Benjamini–Hochberg correction). Asterisks indicate gene names that were not present in the original annotation and instead found through BLAST searches on the *Ovis aries* genome. Genes labelled as 'YAP- and mechanical stiffness-induced genes' are those previously found in [59].

reduction in MVIC NAR (figure 4*d*) is likely to be a direct result of the pronounced radial distension that occurred post MI (figure 3). This is based on our previous work on quantitative relations between the MV leaflet stretch and local MVIC deformations where we quantitatively demonstrated that MVIC deformation can be directly predicted from organ- and tissue-level deformations [23]. Moreover, we noted that alterations in the peak MVIC NAR under cyclic loading has a direct impact on their quantified biosynthetic levels [23,58], with approximately 10% strain being about the level required for the homeostatic level (within the limits of the study), suggesting that deviations from this range may lead to deleterious tissue remodelling.

The RNA sequencing experiments provided unprecedented insight into the transcriptomic changes occurring in response to IMR. Angiotensin (*AGT*) is one of the most significantly and strongly upregulated genes in sheep experiencing IMR at four weeks ($\beta_2 = 2.38$, adjusted *p*-value=0.034), suggesting that the angiotensin-converting enzyme inhibitors (ACEIs) and angiotensin receptor blockers (ARBs) commonly prescribed for coronary artery disease may have additional affects in the MV. In fact, patients tolerating maximal ACEI/ARB therapy exhibit reduced leaflet thickening post MI [34]. Regulator of calcineurin 1 (RCAN1) is elevated at four weeks post MI ($\beta_1 = 2.09$, adjusted *p*-value=0.063), but decreased in the subset of sheep with MR at four weeks post MI ($\beta_2 = -3.07$, adjusted *p*-value=0.0003). RCAN1 inhibits cardiac hypertrophy [61,62] and is a direct transcriptional target of NFATc1 during valvulogenesis [63]. Overexpression of *RCAN1* leads to reduced LV growth/remodelling and reduced collagen deposition at four weeks post MI in a transgenic mouse model [62] while silencing of *RCAN1* increased pulmonary VEC migration in ovine post-natal valves [64]. Ciclosporin A and FK506 are pharmaceuticals that inhibit calcineurin and have profound effects on cardiac hypertrophy, but they were deemed inappropriate for treating cardiac hypertrophy because of nephrotoxicity [65]. Myosin light chain kinase (*MLCK*) is downregulated at four weeks in sheep experiencing MR ($\beta_2 = -2.00$, adjusted *p*-value=0.040) and transgelin (*TAGLN*, SM22) is downregulated ($\beta_3 = -1.14$, adjusted *p*-value=0.022) at eight weeks post MI, which agree with the decrease in NAR observed through histology. *MKI67* is upregulated at four weeks post MI ($\beta_1 = 2.06$, adjusted *p*-value=0.079), a marker previously used to indicate cell proliferation in IMR [25]. Finally, *CXCL9* and *CLEC10A* are the most strongly upregulated genes at four weeks post MI (*CXCL9*: $\beta_1 = 5.96$, adjusted *p*-value=0.003; *CLEC10A*: $\beta_1 = 5.01$, adjusted *p*-value=0.079), indicating a possible attempt to recruit lymphocytes to the MV post MI by dendritic cells [66], similar to the role of *CXCL9* in recruiting T cells to the MV in rheumatic disease [67]. The presence of *LAG3* in sheep exhibiting MR at four weeks post MI ($\beta_2 = 2.95$, adjusted *p*-value=0.005) also points to T-cell infiltration [68], possibly pointing to the same infiltrating cell population found in [25] through staining for CD45. Although there are limited studies investigating the immune response and inflammation cascade involved in the context of IMR, evidence of platelet activation has been observed in MR caused by MV prolapse [69,70], which could also contribute to leukocyte recruitment and activation in IMR.

4.4. Altered mechanotransduction and extracellular matrix organization are major gene groups altered in response to ischaemic mitral regurgitation

In addition to roles of individual genes, grouping genes by promoter or function can provide further insight into the

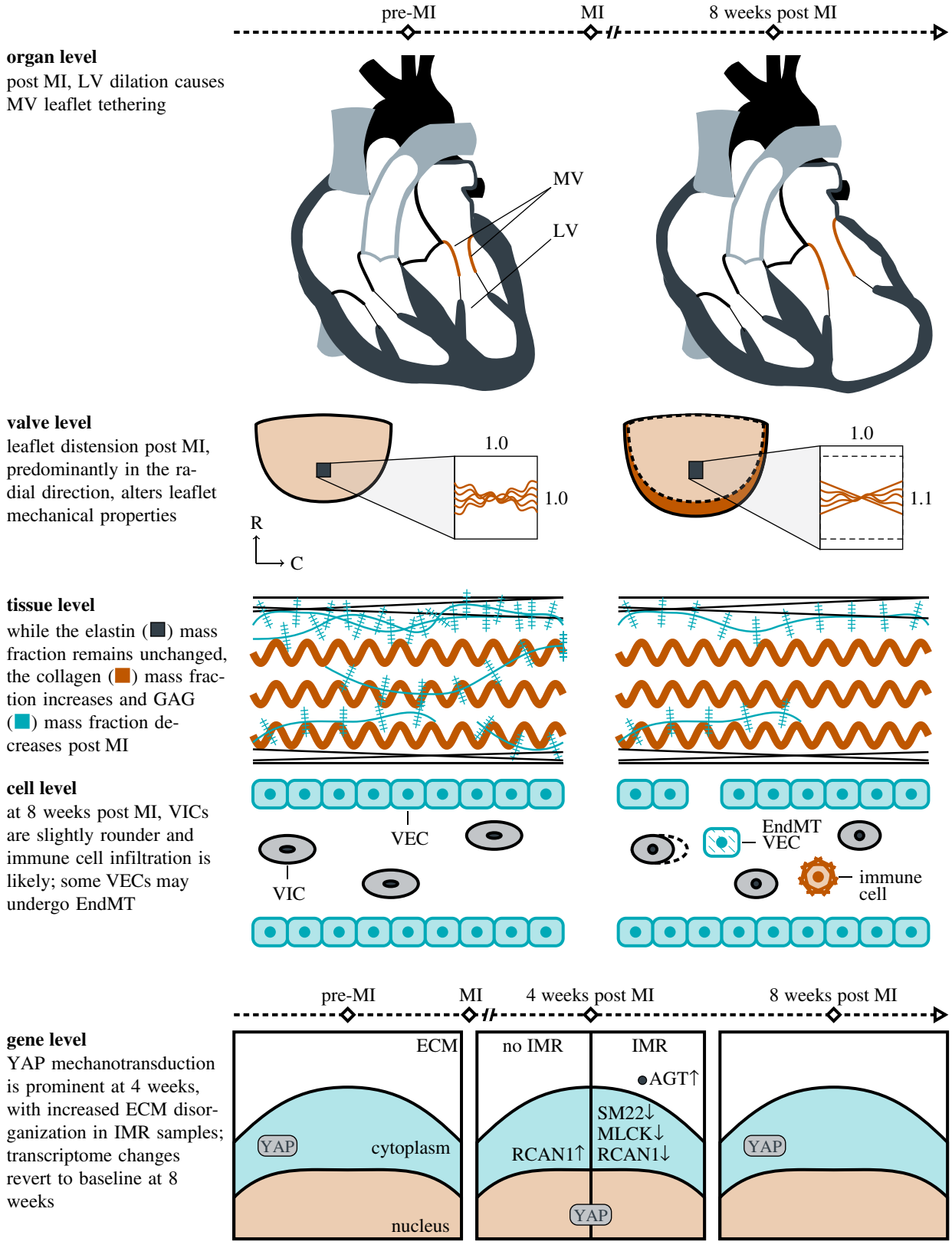

Figure 6. Illustration of the multiscale behaviour of IMR.

function of VICs in IMR. Many of the genes upregulated at four weeks post MI were also found in a previous study comparing genes that are induced both by YAP in NIH 3T3 fibroblasts and mechanical stiffness in human lung fibroblasts [59], indicating increased mechanical activation at four weeks post MI and agreeing with the larger strains observed radially post MI *in vivo* [20]. In the GSEA analysis, decreases in genes related to 'extracellular matrix organization' and 'ECM proteoglycans' obtained by ranking all genes by β_2 agree with protein/tissue-level changes in the overall GAG component of the ECM observed in quantitative histology. These results indicate remarkable consistency across all scales investigated.

4.5. Limitations of the present study

Although this study presented a detailed multiscale view into the mechanism of MV remodelling in IMR, limitations remain.

First, IMR is an intrinsic disease of the LV, so the extent and location of the MI likely influence the observed MV remodelling. In the present study, we controlled for this effect by inducing posterobasal MIs of equal size in all animals. Although this type of MI has substantial clinical relevance, future studies should investigate the sensitivity of MV remodelling phenomena to other types of MI. Next, at the cellular level, there was no effort to separate VICs from VECs or infiltrating immune cells, and conclusions drawn about specific cell types are thus limited. For instance, a constant level of *ACTA2* could either be because IMR did not affect VIC/VEC *ACTA2* expression or an increase in VEC *ACTA2* expression, as observed previously [25,27,34], is balanced by a decrease in VIC *ACTA2* expression. Therefore, the results were only attributed to specific cell types if the gene of interest has a very restricted cell type distribution (e.g. *CLEC10A* for CD1c+ dendritic cells [66]). Finally, we appear to be characterizing initial changes in gene expression and longer term, higher powered studies are needed to elucidate the complete and possibly subtle dynamics of the MVIC response to IMR. The limitations of this study suggest future directions for characterizing MV remodelling in response to IMR.

5. Conclusion and future directions

The multiscale experiments conducted herein are crucial for both improving our understanding of the complex behaviours of the MV in health and disease and developing more biologically informed advanced computational simulations of the MV post MI. Mechanical testing of tissues post MI revealed a critical change in the anisotropy observed in pre-MI valves, consistent with a substantial and permanent radial leaflet distension induced by leaflet tethering. The material composition was also altered, with more collagen, fewer GAGs, and similar elastin compositions. These data can better inform MV material models post MI as one of the three critical pillars of MV *in vivo* simulation post MI [71]. Such computational models promise to suggest optimal device designs and patients suitable for particular treatments. Moreover, connecting to the level of the transcriptome paves the way for multiscale models to extend down to signalling mechanisms with the goal of eventually evaluating both surgical and pharmaceutical interventions in one unified computational framework.

Ethics. All animal protocols used in this study were approved by the University of Pennsylvania's Institutional Animal Care and Use Committee and complied with the National Institute of Health's guidelines for the care and use of laboratory animals (NIH Publication 85-23, revised 1996).

Data accessibility. RNA sequencing data: GEO Series accession no. GSE139921 (www.ncbi.nlm.nih.gov/geo/query/acc.cgi?acc=GSE139921).

Authors' contributions. D.P.H. performed the bioinformatics analysis of the RNA sequencing data and aided in analysis and interpretation of the histology data. B.V.R. analysed and modelled the mechanical testing data and analysed the histology data. D.P.H. and B.V.R. drafted the initial manuscript. E.C. processed leaflets for RNA sequencing. S.A. performed biaxial mechanical testing on MV leaflets. A.H.K. assisted with the quantitative analysis of the histology data. R.C.G. and J.H.G. supervised the animal studies. M.S.S., G.F., J.H.G. and R.C.G. designed the study. All authors provided crucial feedback on the interpretation of the study and revisions to the manuscript. All authors gave final approval for publication and agree to be held accountable for the work performed therein.

Competing interests. We declare we have no competing interest.

Funding. This work was supported by the National Heart, Lung and Blood Institute of the National Institutes of Health (R01-HL119297 to J.H.G. and M.S.S., R01-HL73021 and R01-HL63954 to R.C.G. and J.H.G., R01-HL131872 to G.F. and F31-HL137328 to S.A.); the American Heart Association (18POST33990101 to D.P.H., 18PRE34030258 to B.V.R. and 17PRE33420135 to S.A.); the National Science Foundation (DGE-1610403 to B.V.R.); and the Harry S. Moss Heart Trust.

References

1. Khalighi AH, Drach A, Bloodworth CH, Pierce EL, Yoganathan AP, Gorman RC, Gorman JH, Sacks MS. 2017 Mitral valve chordae tendineae: topological and geometrical characterization. *Ann. Biomed. Eng.* **45**, 378–393. (doi:10.1007/s10439-016-1775-3)
2. Khalighi AH, Drach A, Gorman RC, Gorman JH, Sacks MS. 2018 Multi-resolution geometric modeling of the mitral heart valve leaflets. *Biomech. Model. Mechanobiol.* **17**, 351–366. (doi:10.1007/s10237-017-0965-8)
3. Drach A, Khalighi AH, Sacks MS. 2017 A comprehensive pipeline for multi-resolution modeling of the mitral valve: validation, computational efficiency, and predictive capability. *Int. J. Numer. Methods Biomed. Eng.* **34**, e2921. (doi:10.1002/cnm.2921)
4. Benjamin EJ *et al.* 2019 Heart disease and stroke statistics—2019 update: a report from the American Heart Association. *Circulation* **139**, e56–e528. (doi:10.1161/CIR.0000000000000659)
5. Bursi F, Enriquez-Sarano M, Nkomo VT, Jacobsen SJ, Weston SA, Meverden RA, Roger VL. 2005 Heart failure and death after myocardial infarction in the community. *Circulation* **111**, 295–301. (doi:10.1161/01.CIR.0000151097.30779.04)
6. Pérez de Isla L *et al.* 2007 Functional mitral regurgitation after a first non-ST-segment elevation acute coronary syndrome: contribution to congestive heart failure. *Eur. Heart J.* **28**, 2866–2872. (doi:10.1093/eurheartj/ehm469)
7. Lamas GA, Mitchell GF, Flaker GC, Smith SC, Gersh BJ, Basta L, Moyé L, Braunwald E, Pfeffer MA. 1997 Clinical significance of mitral regurgitation after acute myocardial infarction. *Circulation* **96**, 827–833. (doi:10.1161/01.CIR.96.3.827)
8. Beeri R *et al.* 2008 Mitral regurgitation augments post-myocardial infarction remodeling: failure of hypertrophic compensation. *J. Am. Coll. Cardiol.* **51**, 476–486. (doi:10.1016/j.jacc.2007.07.093)
9. Grigioni F, Enriquez-Sarano M, Zehr KJ, Bailey KR, Tajik AJ. 2001 Ischaemic mitral regurgitation: long-term outcome and prognostic implications with quantitative Doppler assessment. *Circulation* **103**, 1759–1764. (doi:10.1161/01.CIR.103.13.1759)
10. Sannino A, Smith RL, Schiattarella GG, Trimarco B, Esposito G, Grayburn PA. 2017 Survival and cardiovascular outcomes of patients with secondary mitral regurgitation: a systematic review and meta-analysis. *JAMA Cardiol.* **2**, 1130–1139. (doi:10.1001/jamacardio.2017.2976)
11. Wang J, Gu C, Gao M, Yu W, Yu Y. 2015 Mitral valve replacement therapy causes higher 30-day postoperative mortality than mitral valvuloplasty in patients with severe ischaemic mitral regurgitation: a meta-analysis of 12 studies. *Int. J. Cardiol.* **185**, 304–307. (doi:10.1016/j.ijcard.2015.03.170)
12. Acker MA *et al.* 2014 Mitral-valve repair versus replacement for severe ischaemic mitral regurgitation. *N. Engl. J. Med.* **370**, 23–32. (doi:10.1056/NEJMoa1312808)
13. Goldstein D *et al.* 2016 Two-year outcomes of surgical treatment of severe ischaemic mitral regurgitation. *N. Engl. J. Med.* **374**, 344–353. (doi:10.1056/NEJMoa1512913)
14. Stone GW *et al.* 2018 Transcatheter mitral-valve repair in patients with heart failure. *N. Engl. J. Med.* **379**, 2307–2318. (doi:10.1056/NEJMoa1806640)
15. Grande-Allen KJ, Borowski AG, Troughton RW, Houghtaling PL, Dipaola NR, Moravec CS, Vesely I,

Griffin BP. 2005 Apparently normal mitral valves in patients with heart failure demonstrate biochemical and structural derangements: an extracellular matrix and echocardiographic study. *J. Am. Coll. Cardiol.* **45**, 54–61. (doi:10.1016/j.jacc.2004.06.079)

16. Quick DW, Kunzelman KS, Kneebone JM, Cochran RP. 1997 Collagen synthesis is upregulated in mitral valves subjected to altered stress. *ASAIO J.* **43**, 181–186.
17. Chaput M, Handschumacher MD, Guerrero JL, Holmvang G, Dal-Bianco JP, Sullivan S, Vlahakes GJ, Hung J, Levine RA. 2009 Mitral leaflet adaptation to ventricular remodeling: prospective changes in a model of ischaemic mitral regurgitation. *Circulation* **120**, S99–S103. (doi:10.1161/CIRCULATIONAHA.109.844019)
18. Dal-Bianco JP *et al.* 2009 Active adaptation of the tethered mitral valve: insights into a compensatory mechanism for functional mitral regurgitation. *Circulation* **120**, 334–342. (doi:10.1161/CIRCULATIONAHA.108.846782)
19. Suh YJ, Chang BC, Im DJ, Kim YJ, Hong YJ, Hong GR, Kim YJ. 2015 Assessment of mitral annuloplasty ring by cardiac computed tomography: correlation with echocardiographic parameters and comparison between two different ring types. *J. Thorac. Cardiovasc. Surg.* **150**, 1082–1090. (doi:10.1016/j.jtcvs.2015.07.019)
20. Rego BV. 2019 Remodeling of the mitral valve: an integrated approach for predicting long-term outcomes in disease and repair. PhD dissertation, The University of Texas at Austin, Austin, TX, USA.
21. Cerfolio RJ, Orszulak TA, Pluth JR, Harmsen WS, Schaff HV. 1996 Reoperation after valve repair for mitral regurgitation: early and intermediate results. *J. Thorac. Cardiovasc. Surg.* **111**, 1177–1184. (doi:10.1016/S0022-5223(96)70219-2)
22. Khang A, Buchanan RM, Ayoub S, Rego BV, Lee CH, Ferrari G, Anseth KS, Sacks MS. 2018 Mechanobiology of the heart valve interstitial cell: simulation, experiment, and discovery. In *Mechanobiology in Health and Disease* (ed. SW Verbruggen), pp. 249–283. London, UK: Elsevier.
23. Ayoub S, Lee CH, Driesbaugh KH, Anselmo W, Hughes CT, Ferrari G, Gorman RC, Gorman JH, Sacks MS. 2017 Regulation of valve interstitial cell homeostasis by mechanical deformation: implications for heart valve disease and surgical repair. *J. R. Soc. Interface* **14**, 20170580. (doi:10.1098/rsif.2017.0580)
24. Sielicka A *et al.* 2018 Pathological remodeling of mitral valve leaflets from unphysiologic leaflet mechanics after undersized mitral annuloplasty to repair ischaemic mitral regurgitation. *J. Am. Heart Assoc.* **7**, e009777. (doi:10.1161/JAHA.118.009777)
25. Dal-Bianco JP *et al.* 2016 Myocardial infarction alters adaptation of the tethered mitral valve. *J. Am. Coll. Cardiol.* **67**, 275–287. (doi:10.1016/j.jacc.2015.10.092)
26. Ávila Vanzzini N *et al.* 2018 Clinical and echocardiographic factors associated with mitral plasticity in patients with chronic inferior myocardial infarction. *Eur. Heart J.-Cardiovasc. Imaging* **19**, 508–515. (doi:10.1093/ehjci/jey021)
27. Bartko PE *et al.* 2017 Effect of losartan on mitral valve changes after myocardial infarction. *J. Am. Coll. Cardiol.* **70**, 1232–1244. (doi:10.1016/j.jacc.2017.07.734)
28. Gorman RC, McCaughan JS, Ratcliffe MB, Gupta KB, Streicher JT, Ferrari VA, St John-Sutton MG, Bogen DK, Edmunds Jr LH. 1995 Pathogenesis of acute ischaemic mitral regurgitation in three dimensions. *J. Thorac. Cardiovasc. Surg.* **109**, 684–693. (doi:10.1016/S0022-5223(95)70349-7)
29. Gorman III JH, Gorman RC, Jackson BM, Hiramatsu Y, Gikakis N, Kelley ST, Sutton MG, Plappert T, Edmunds Jr LH. 1997 Distortions of the mitral valve in acute ischaemic mitral regurgitation. *Ann. Thorac. Surg.* **64**, 1026–1031. (doi:10.1016/S0003-4975(97)00850-3)
30. Kim DH, Morris B, Guerrero JL, Sullivan SM, Hung J, Levine RA. 2018 *Experimental models of cardiovascular diseases: methods and protocols*, pp. 295–308. New York, NY: Springer.
31. Gorman JH, Gorman RC, Jackson BM, Enomoto Y, St John-Sutton MG, Edmunds L. 2003 Annuloplasty ring selection for chronic ischaemic mitral regurgitation: lessons from the ovine model. *Ann. Thorac. Surg.* **76**, 1556–1563. (doi:10.1016/S0003-4975(03)00891-9)
32. Wilson EM *et al.* 2003 Region- and type-specific induction of matrix metalloproteinases in post-myocardial infarction remodeling. *Circulation* **107**, 2857–2863. (doi:10.1161/01.CIR.0000068375.40887.FA)
33. Ifkovits JL, Tous E, Minakawa M, Morita M, Robb JD, Koomalsingh KJ, Gorman JH, Gorman RC, Burdick JA. 2010 Injectable hydrogel properties influence infarct expansion and extent of postinfarction left ventricular remodeling in an ovine model. *Proc. Natl Acad. Sci. USA* **107**, 11 507–11 512. (doi:10.1073/pnas.1004097107)
34. Beaudoin J *et al.* 2017 Mitral leaflet changes following myocardial infarction. *Circ. Cardiovasc. Imaging* **10**, e006512. (doi:10.1161/CIRCIMAGING.117.006512)
35. May-Newman K, Yin FC. 1995 Biaxial mechanical behavior of excised porcine mitral valve leaflets. *Am. J. Physiol.* **269**, H1319–H1327.
36. Grashow JS, Sacks MS, Liao J, Yoganathan AP. 2006 Planar biaxial creep and stress relaxation of the mitral valve anterior leaflet. *Ann. Biomed. Eng.* **34**, 1509–1518. (doi:10.1007/s10439-006-9183-8)
37. Grashow JS, Yoganathan AP, Sacks MS. 2006 Biaxial stress-stretch behavior of the mitral valve anterior leaflet at physiologic strain rates. *Ann. Biomed. Eng.* **34**, 315–325. (doi:10.1007/s10439-005-9027-y)
38. Zhang W, Ayoub S, Liao J, Sacks MS. 2016 A meso-scale layer-specific structural constitutive model of the mitral heart valve leaflets. *Acta Biomater.* **32**, 238–255. (doi:10.1016/j.actbio.2015.12.001)
39. Lee CH, Zhang W, Liao J, Carruthers CA, Sacks JI, Sacks MS. 2015 On the presence of affine fibril and fiber kinematics in the mitral valve anterior leaflet. *Biophys. J.* **108**, 2074–2087. (doi:10.1016/j.bpj.2015.03.019)
40. Fan R, Sacks MS. 2014 Simulation of planar soft tissues using a structural constitutive model: finite element implementation and validation. *J. Biomech.* **47**, 2043–2054. (doi:10.1016/j.jbiomech.2014.03.014)
41. Rego BV, Wells SM, Lee CH, Sacks MS. 2016 Mitral valve leaflet remodelling during pregnancy: insights into cell-mediated recovery of tissue homeostasis. *J. R. Soc. Interface* **13**, 20160709. (doi:10.1098/rsif.2016.0709).
42. Sacks MS, Zhang W, Wognum S. 2016 A novel fibre-ensemble level constitutive model for exogenous cross-linked collagenous tissues. *Interface Focus* **6**, 20150090. (doi:10.1098/rsfs.2015.0090)
43. Billiar KL, Sacks MS. 2000 Biaxial mechanical properties of the native and glutaraldehyde-treated aortic valve cusp: Part II — a structural constitutive model. *J. Biomech. Eng.* **122**, 327–335. (doi:10.1115/1.1287158)
44. Merryman WD, Lukoff HD, Long RA, Engelmayr Jr GC, Hopkins RA, Sacks MS. 2007 Synergistic effects of cyclic tension and transforming growth factor-β1 on the aortic valve myofibroblast. *Cardiovasc. Pathol.* **16**, 268–276. (doi:10.1016/j.carpath.2007.03.006)
45. Balachandran K, Konduri S, Sucosky P, Jo H, Yoganathan A. 2006 An ex vivo study of the biological properties of porcine aortic valves in response to circumferential cyclic stretch. *Ann. Biomed. Eng.* **34**, 1655–1665. (doi:10.1007/s10439-006-9167-8)
46. Rego BV, Sacks MS. 2017 A functionally graded material model for the transmural stress distribution of the aortic valve leaflet. *J. Biomech.* **54**, 88–95. (doi:10.1016/j.jbiomech.2017.01.039)
47. Yezzi A, Prince J. 2003 An Eulerian PDE approach for computing tissue thickness. *IEEE Trans. Med. Imaging* **22**, 1332–1339. (doi:10.1109/TMI.2003.817775)
48. Pawlowsky-Glahn V, Buccianti A. 2011 *Compositional data analysis: theory and applications*. Chichester, UK: John Wiley & Sons.
49. Huber W *et al.* 2015 Orchestrating high-throughput genomic analysis with bioconductor. *Nat. Methods* **12**, 115–121. (doi:10.1038/nmeth.3252)
50. Durinck S, Spellman PT, Birney E, Huber W. 2009 Mapping identifiers for the integration of genomic datasets with the R/Bioconductor package biomaRt. *Nat. Protocols* **4**, 1184–1191. (doi:10.1038/nprot.2009.97)
51. Love MI, Huber W, Anders S. 2014 Moderated estimation of fold change and dispersion for RNA-seq data with DESeq2. *Genome Biol.* **15**, 550. (doi:10.1186/s13059-014-0550-8)
52. Zhu A, Ibrahim JG, Love MI. 2018 Heavy-tailed prior distributions for sequence count data: removing the noise and preserving large differences. *Bioinformatics* **35**, 2084–2092. (doi:10.1093/bioinformatics/bty895)
53. Benjamini Y, Hochberg Y. 1995 Controlling the false discovery rate: a practical and powerful approach to multiple testing. *J. R. Stat. Soc. B (Methodological)* **57**, 289–300. (doi:10.1111/j.2517-6161.1995.tb02031.x)
54. Subramanian A *et al.* 2005 Gene set enrichment analysis: a knowledge-based approach for interpreting genome-wide expression profiles. *Proc.*

Natl Acad. Sci. USA **102**, 15 545–15 550. (doi:10.1073/pnas.0506580102)

55. Fabregat A *et al.* 2018 The Reactome pathway knowledgebase. *Nucleic Acids Res.* **46**, D649–D655. (doi:10.1093/nar/gkx1132)
56. Yu G, He QY. 2016 ReactomePA: an R/Bioconductor package for Reactome pathway analysis and visualization. *Mol. Biosyst.* **12**, 477–479. (doi:10.1039/C5MB00663E)
57. Edgar R, Domrachev MELA. 2002 Gene expression omnibus: NCBI gene expression and hybridization array data repository. *Nucleic Acids Res.* **30**, 207–210. (doi:10.1093/nar/30.1.207)
58. Lee CH, Zhang W, Feaver K, Gorman RC, Gorman JH, Sacks MS. 2017 On the *in vivo* function of the mitral heart valve leaflet: insights into tissue-interstitial cell biomechanical coupling. *Biomech. Model. Mechanobiol.* **16**, 1613–1632. (doi:10.1007/s10237-017-0908-4)
59. Liu F *et al.* 2014 Mechanosignaling through YAP and TAZ drives fibroblast activation and fibrosis. *Am. J. Physiol.-Lung Cellular Mol. Physiol.* **308**, L344–L357. (doi:10.1152/ajplung.00300.2014)
60. Rego BV, Khalighi AH, Drach A, Lai EK, Pouch AM, Gorman RC, Gorman JH, Sacks MS. 2018 A noninvasive method for the determination of *in vivo* mitral valve leaflet strains. *Int. J. Numer. Methods Biomed. Eng.* **34**, e3142. (doi:10.1002/cnm.3142)
61. Rothermel BA *et al.* 2001 Myocyte-enriched calcineurin-interacting protein, MCIP1, inhibits cardiac hypertrophy *in vivo*. *Proc. Natl Acad. Sci. USA* **98**, 3328–3333. (doi:10.1073/pnas.041614798)
62. van Rooij E *et al.* 2004 MCIP1 overexpression suppresses left ventricular remodeling and sustains cardiac function after myocardial infarction. *Circ. Res.* **94**, e18–e26. (doi:10.1161/01.RES.0000118597.54416.00)
63. Wu H, Kao Sc, Barrientos T, Baldwin SH, Olson EN, Crabtree GR, Zhou B, Chang CP. 2007 Down syndrome critical region-1 is a transcriptional target of nuclear factor of activated T cells-c1 within the endocardium during heart development. *J. Biol. Chem.* **282**, 30673–30679. (doi:10.1074/jbc.M703622200)
64. Jang GH, Park IS, Yang JH, Bischoff J, Lee YM. 2010 Differential functions of genes regulated by VEGF-NFATc1 signaling pathway in the migration of pulmonary valve endothelial cells. *FEBS Lett.* **584**, 141–146. (doi:10.1016/j.febslet.2009.11.031)
65. Kuhn C, Hille S, Frey N. 2015 Molecular targets in the treatment of cardiac hypertrophy. In *Pathophysiology and pharmacotherapy of cardiovascular disease* (eds G Jagadeesh, P Balakumar, K Maung-U), pp. 343–371. New York, NY: Springer.
66. Heger L *et al.* 2018 CLEC10a is a specific marker for human CD1c+ dendritic cells and enhances their toll-like receptor 7/8-induced cytokine secretion. *Front. Immunol.* **9**, 744. (doi:10.3389/fimmu.2018.00744)
67. Faé KC *et al.* 2013 CXCL9/Mig mediates T cells recruitment to valvular tissue lesions of chronic rheumatic heart disease patients. *Inflammation* **36**, 800–811. (doi:10.1007/s10753-013-9606-2)
68. Su L, Hu A, Luo Y, Zhou W, Zhang P, Feng Y. 2014 HMGN2, a new anti-tumor effector molecule of $CD8^+$ T cells. *Mol. Cancer* **13**, 178. (doi:10.1186/1476-4598-13-178)
69. Tse HF, Lau CP, Cheng G. 1997 Relation between mitral regurgitation and platelet activation. *J. Am. Coll. Cardiol.* **30**, 1813–1818. (doi:10.1016/S0735-1097(97)00380-X)
70. Tan HT, Ling LH, Dolor-Torres MC, Yip JWL, Richards AM, Chung MCM. 2013 Proteomics discovery of biomarkers for mitral regurgitation caused by mitral valve prolapse. *J. Proteomics* **94**, 337–345. (doi:10.1016/j.jprot.2013.10.009)
71. Sacks MS *et al.* 2019 On the simulation of mitral valve function in health, disease, and treatment. *J. Biomech. Eng.* **141**, 070804. (doi:10.1115/1.4043552)